Examination of nanosecond laser melting thresholds in refractory metals by shear wave acoustics

A. Abdullaev,[1,a,b] B. Muminov,[1,a] A. Rakhymzhanov,[2,3,a] N. Mynbayev,[2,3,a] and Z. N. Utegulov[1,2,b]

[1]*Department of Physics, School of Science and Technology, Nazarbayev University, Astana 010000, Kazakhstan*

[2]*Center for Energy and Advanced Material Science, National Laboratory Astana, Nazarbayev University, Astana 010000, Kazakhstan*

[3]*L.N.Gumilyov Eurasian National University, Astana 010008, Kazakhstan*

(Received 3 October 2016; accepted 29 June 2017; published online 12 July 2017)

Nanosecond laser pulse-induced melting thresholds in refractory (Nb, Mo, Ta and W) metals are measured using detected laser-generated acoustic shear waves. Obtained melting threshold values were found to be scaled with corresponding melting point temperatures of investigated materials displaying dissimilar shearing behavior. The experiments were conducted with motorized control of the incident laser pulse energies with small and uniform energy increments to reach high measurement accuracy and real-time monitoring of the epicentral acoustic waveforms from the opposite side of irradiated sample plates. Measured results were found to be in good agreement with numerical finite element model solving coupled elastodynamic and thermal conduction governing equations on structured quadrilateral mesh. Solid-melt phase transition was handled by means of apparent heat capacity method. The onset of melting was attributed to vanished shear modulus and rapid radial molten pool propagation within laser-heated metal leading to preferential generation of transverse acoustic waves from sources surrounding the molten mass resulting in the delay of shear wave transit times. Developed laser-based technique aims for applications involving remote examination of rapid melting processes of materials present in harsh environment (e.g. spent nuclear fuels) with high spatio-temporal resolution. [http://dx.doi.org/10.1063/1.4993591]

I. INTRODUCTION

The laser-based generation and detection of ultrasound waves have been widely used to characterize materials remotely and non-destructively. Due to noncontact nature of these measurements, the opportunity to employ laser-based techniques for non-contact, *in-situ* control of materials and processes present in harsh environments has found numerous research and industrial applications. Considering above mentioned advantages, this technique can be also used for advanced examination of fresh and post-irradiated nuclear reactor fuels during fast melting regime. Rose[1] and Doyle[2] theoretically considered acoustic surface sources whose model present fairly good description of displacement waveforms for solid plate along epicentral direction due to bulk ultrasonic waves generated by laser pulse irradiation. However, experimental results clearly show the existence of so called "precursor" peak which cannot be observed using surface sources only. As was shown by Telschow,[3] the precursor peak is caused by spatial distribution of sub-surface heat diffusion and finite optical penetration.

[a]These authors have made equal contribution

[b]azat.abdullaev@nu.edu.kz, zhutegulov@nu.edu.kz (Authors to whom correspondence should be addressed)

There has been a number of works devoted to laser pulsed generation of acoustic waves in thermoelastic and ablative regimes in metals.[4–12] However, limited attention has been paid to laser ultrasonic regime when the laser pulse energy is sufficient to melt solids but not enough to ablate them. Previously few researchers have investigated signal amplitude changes for shear acoustic waves in AISI 304 stainless steel[13] and for surface acoustic waves in silicon[14] under nanosecond laser-induced melting, with recent work on Si melting using time-resolved sub-nanosecond reflectometry.[15] Recently we have examined epicentral waveform for laser ultrasound in the surface melting regime of tungsten without automated control of incident laser pulse energy[16] and performed numerical simulations based on finite element model (FEM) of epicentral displacement.[17–19] Time resolved spectral pyrometry was used to measure melting points of stainless steel and platinum using nanosecond laser heating.[20] There has also been intense research devoted to measure melting points of refractory materials using laser pulses on the scale of milliseconds[21–23] and microseconds.[24]

In this work we have introduced *automated control* of laser pulse energy-induced melting to improve measurement accuracy by studying dynamic thermomechanical properties in thermoelastic regime, at and above melting in *several refractory metals* such as (niobium, molybdenum, tantalum and tungsten) with various bulk shearing behavior, by actually *measuring nanosecond laser melting thresholds* in these metals. From the measurements we consistently observed an increase in the propagation time of acoustic shear waves with the increase of the incident laser peak power density. *Compared to our previous results,*[16–19] *in the present work we have improved quantitative convergence between our experimental results on peak intensity-dependent shear wave arrival time and the finite element model (FEM)* solving coupled elastodynamic and thermal conduction governing equations with solid-melt phase transition using apparent heat capacity method.[25] Developed model shows that laser-induced surface melting and corresponding complete loss of rigidity (i.e. vanishing of shear modulus) within molten pool along with rapid radially spreading molten mass results in the shear wave arrival delay, which was found to be due to generation of *surface and volumetric thermoelastic sources from the heated zone surrounding the molten pool*.

II. THEORY AND NUMERICAL MODEL

In this work we treat laser-generated ultrasound via coupled thermal conduction and elastic wave equations:[26]

$$\rho C_v(\partial T/\partial t) + \rho C_v \boldsymbol{u_1} \boldsymbol{\nabla} T = \boldsymbol{\nabla}(k \boldsymbol{\nabla} T) + Q, \tag{1}$$

$$(\lambda + G)\,\boldsymbol{\nabla}(\boldsymbol{\nabla} \boldsymbol{u_1}) - G\boldsymbol{\nabla} \times \boldsymbol{\nabla} \times \boldsymbol{u_1} - \rho\left(\partial^2 \boldsymbol{u_1}/\partial t^2\right) = \alpha(3\lambda + 2G)\boldsymbol{\nabla} T, \tag{2}$$

where λ is the first Lame coefficient, G is the shear modulus, T is material temperature, k is the thermal conductivity, ρ is the density, C_v is the volume specific heat, $\boldsymbol{u}_1$ is the displacement vector caused by thermal expansion (within laser irradiated region) and corresponding stresses, α is thermal expansion coefficient and Q is absorbed laser-induced spatio-temporal power density (in W/m^3). The right side of Eq. 2 represents external force per unit volume associated with laser-induced temperature gradient in the sub-surface volume of heated region. C_v is the "effective" specific heat defined by the "effective heat capacity method" for melting and melt-solid interface,[25]:

$$C_v = C_{solid}(1 - a\,(T)) + C_{liquid} a(T) + q_L \frac{da}{dT}, \tag{3}$$

where C_{solid} and C_{liquid} are specific heats of solid and melt phases, respectively, and q_L is the latent heat of melting taken into account by increasing the heat capacity of the material near the metal-melt phase temperature ($T_m \pm 10$ K), and $0 \leq a(T) \leq 1$ is a fraction of melt in solid-melt binary mixture. Equation coefficients (λ, G, ρ, C_v, k, α) are treated as temperature dependent functions, which are interpolated and extrapolated over temperature range using tabulated values.[27–30] All studied metals were assumed to be thermally and elastically isotropic.

Spatio-temporal laser heat source was assumed to be of the following form:

$$Q(r, z, t) = Q_0 t e^{-t/\tau} e^{-r^2/2\delta^2} e^{-\beta z}, \tag{4}$$

where t – time (for $t > 0$); r – radial distance in the plane of the sample; τ and δ – constants representing laser's pulse duration and beam diameter correspondingly; z – the vertical distance measured from the sample surface ($z \geq 0$) and β - metal's optical absorption coefficient.

Since maximum heat propagation distance along laser-heated sample's vertical direction is typically on the order of 1 μm[17] below the surface, which was calculated using following equation:

$$l_{pen} = \sqrt{4\kappa\tau}, \tag{5}$$

where κ – thermal diffusivity and τ – laser pulse duration, we set a two-dimensional axisymmetric FEM with structured non-uniform mesh which has considerably high spatial resolution of 0.5 - 3 nm for thermal conduction in laser irradiated near-surface region and reasonably low spatially resolved mesh of 0.5 - 2 μm for the scale of acoustic wave propagation across 1.5 mm thick metal plates under study. Time steps were ranging from 1 ps during heat propagation in near surface region at the onset of laser pulse irradiation to 100 ps when heat source has been weakened to $1/e^2$ of initial intensity. Such adaptive choice of computational grid allowed us to spatially resolve thermo-mechanical processes without resorting to extensive computation time. In order to achieve numerical stability of our FEM simulations, upon the onset of laser-induced melting the sharp step-like transition in density and bulk shear moduli of heated metals has been numerically "smoothened" over finite temperature span ($T_{melt} \pm 10$ K). In contrast to Rose model,[1] where surface acoustic sources were used, we engaged surface and volume distributed sources within laser-irradiated region with the help of optimized mesh quality which allowed us to conduct quantitative investigations of time arrivals of propagated shear and longitudinal bulk waves.

III. EXPERIMENT

The experimental setup is shown in Figure 1. We used Nd:YAG Q-switched laser of 5.2 ns pulse duration (FWHM) with a pulse jitter of less than 1 ns, second harmonic wavelength of 532 nm operating at the repetition rate of 10 Hz to generate ultrasound waves in studied metals. We investigated 4 different high purity polycrystalline refractory metal plates of niobium (Nb), molybdenum (Mo), tantalum (Ta) and tungsten (W) with plate dimensions of 60 mm x 60 mm x 1.5 mm. To detect ultrasound waves the laser vibrometer based on two-wave mixing photorefractive interferometry with 2.5 GHz bandwidth[31] was employed. The experiments were performed with motorized stepper motor to control the incident laser pulse energy with in-situ measurement of varying laser pulse energy by energy meter and acoustic waveforms detected by the laser vibrometer on the opposite side of 1.5

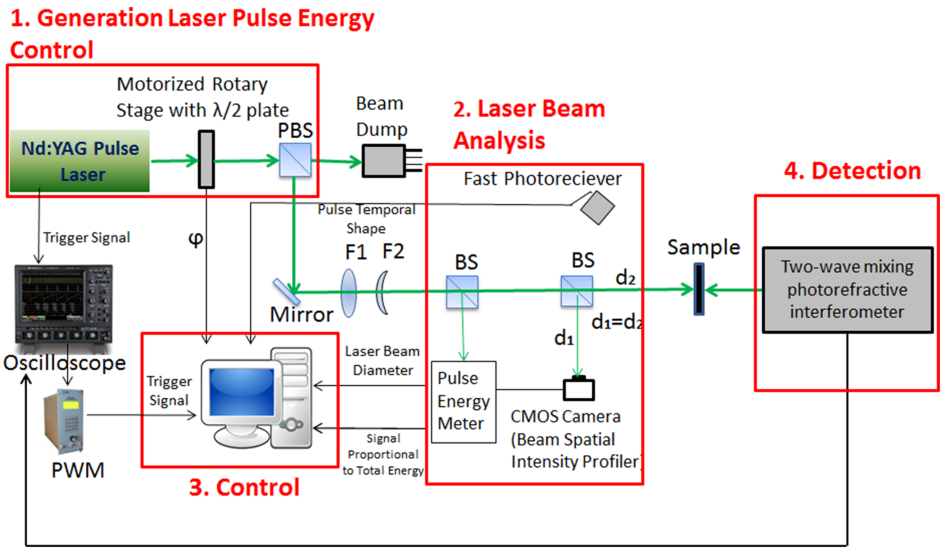

FIG. 1. Experimental setup constructed for in-situ measurements of laser pulse energies and epicentral acoustic waveforms in metal plates irradiated by nanosecond laser pulses.

mm thick plates along their epicentral direction using detection laser beam (of ~ 75 μm diameter) focused on sample plates. The combination of plano-concave (f = 150 mm) and plano-convex (f = -50 mm) lenses was used to control collimation of the incident laser beam. The Gaussian beam diameter of 0.9 mm obtained from spatial intensity profile was measured by a high-resolution digital CMOS beam profiling camera. A beam splitter with known split ratio was used to determine incident beam pulse energy. To ensure the accurate measurement of the laser beam diameter in the plane of the sample surface, the distance d2 from the beam splitter to the sample and the distance d1 from the beam splitter to beam view camera were kept equal and laser beams in these two paths were collimated. To generate acoustic waves in thermoelastic and melting regimes, the incident pulse energy on the sample was gradually increased by passing the beam through half wave-plate (mounted on vertical rotation stage) and polarizing beam splitter cube. This was achieved by gradual rotation of the polarization direction of linearly polarized light. To reach constant incremental steps (of 10 μJ) in the increased energy of the incoming laser pulses the rotational motion of half wave-plate was automated using motorized stepper motor. The incident pulse energy was gradually increased up to ~ 3 mJ. The computer-controlled closed loop attenuator set and maintained the pulse energy by positioning the half wave-plate based on a feedback signal from the energy meter. The stepper motor driver was controlled using Simulink.

Laser generated ultrasonic signal was detected from the opposite side of the sample plate along its epicentral direction. High bandwidth oscilloscope was used to collect and synchronize the ultrasonic signals from two-wave mixing photorefractive interferometer and trigger signal from the generation laser. The pulse width modulator (PWM), was used to convert a 20 μs input trigger signal into TTL signal with 10 μs pulse width for energy meter and 4 ms pulse width signal for computer at constant frequency. Post-measurement processing included averaging of 400 epicentral waveforms and then fitting epicentral waveforms with high order polynomial.

IV. RESULTS AND DISCUSSION

Our typical measured laser-generated epicentral waveform for tungsten plate in thermoelastic regime along with its FEM fit are shown in Figure 2, which closely mimic earlier obtained result for this metal.[16] The transit time for the longitudinal acoustic (LA) wave propagation across sample plate is ~ 300 ns, as defined by the time interval spanned between the trigger pulse and precursor (i.e. LA peak), while the shear (or transverse acoustic) arrival time, estimated to be ~ 540 ns, is defined by the time interval spanned between the trigger pulse and the downward step (i.e. TA peak).

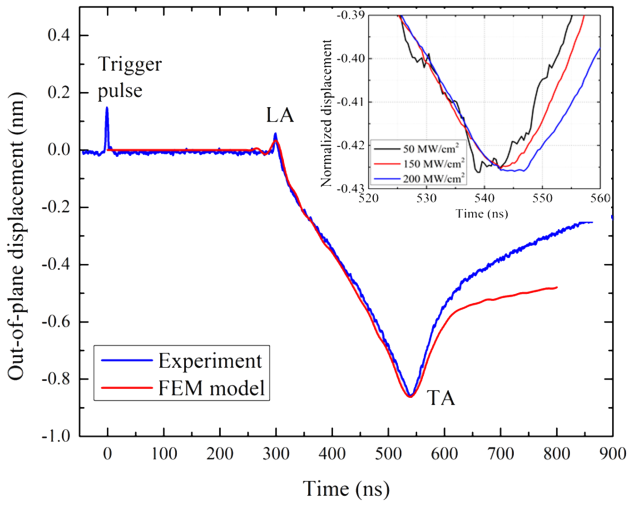

FIG. 2. Measured and theoretical FEM laser-generated epicentral acoustic waveform (normalised to the same units) in tungsten plate. The inset shows epicentral *time delay* of TA waves in thermoelastic and melting regimes.

LA displacement in the positive direction is caused by volume sources which are in turn present because laser-induced heat penetration depth is finite and its amplitude is determined by this depth. According to Telschow[3] the precursor peak in general arises due to finite optical penetration and subsurface thermal diffusion. However, in ceramics and non-metals the subsurface acoustic sources are produced by sizeable optical penetration and in metallic and opaque materials these sources are produced by thermal diffusion because optical penetration depth in them is very small. Precursor peak caused by limited thermal diffusion length is extremely narrow and therefore it is weak compared to the TA out-of-plane displacement.

The inset of Figure 2 shows zoomed region of normalized epicentral waveform near shear wave arrivals during thermoelastic (50 MW/cm^2) and above melting (150 and 200 MW/cm^2) regimes, which are in agreement with earlier measurements in tungsten.[16] The delay in shear wave arrival displayed in the inset is clearly seen upon laser-induced metal-to-liquid phase transition. Shear wave arrival times were determined from the 6th order polynomial fitting of the minima of corresponding signals averaged over 400 acquired epicentral waveforms using high speed oscilloscope. For 150 MW/cm^2 which is just above melting point, this delay is around 1 ns but with further increase of the peak intensity up to 200 MW/cm^2, the observed delay reaches around 4 ns as shown in the inset of Figure 2.

We measured melting threshold of different refractory metals as shown in Figure 3. It shows shear wave arrival times for different refractory metals as a function of incident peak intensity defined by

$$I_{inc} = \frac{4E_{inc}}{\pi D_{beam}^2 \tau_{FWHM}}, \tag{6}$$

where E_{inc}, D_{beam} and τ_{FWHM} are pulse energy, Gaussian beam diameter and pulse duration of the incident laser radiation, respectively.

From Figure 3 it is seen that in thermoelastic regime for all metals the shear wave arrival time remains generally constant. However, after reaching certain incident peak intensity, a clear delay in the shear arrival time is observed, which was earlier attributed to the loss of rigidity within molten

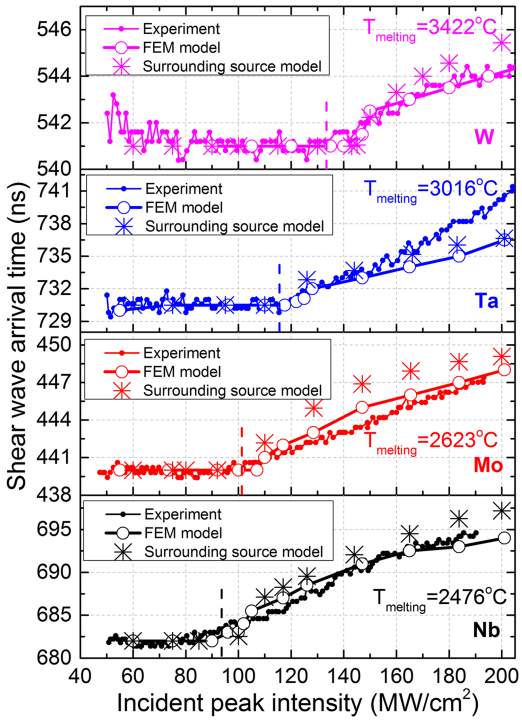

FIG. 3. Measured and FEM computed shear wave arrival times below and above melting thresholds (shown by corresponding vertical dashed lines) versus incident laser peak intensities for different refractory metals.

mass.[16–19] From the measured time delays we estimate the pulsed laser-induced melting thresholds to be at 94, 101, 114 and 134 MW/cm^2 for Nb, Mo, Ta and W, respectively. This increasing trend for melting peak intensity thresholds is in agreement with corresponding increase of handbook melting point temperatures[32] of these solids, as displayed in Figure 3. It should be noted that the melting threshold depends on several parameters including material's optical reflectivity, surface quality and laser pulse duration. However, in the first order approximation, the melting threshold is independent of laser pulse duration due to relatively small heat penetration depth.[33]

In Table I we list measured and numerically predicted melting thresholds for above given metals along with their handbooks values of Poisson's ratios.[34] Experimentally measured melting thresholds (I_{melt}^{exp}) were obtained using polynomial fit intersections between the horizontal baseline (i.e. thermoelastic regime) and take-off curve (i.e. above-melting regime). In Table I we also list two theoretically calculated melting thresholds corresponding to: (1) disappearance of shear modulus (I_{melt}^{G}) and (2) delay of the shear wave arrival time ($I_{melt}^{t_{shear\ delay}}$) across the entire metal plates versus the incident peak intensity. A small discrepancy between experimental and theoretical values of melting thresholds takes place as seen from Table I. To achieve better agreement between simulation and experimental results, we have adjusted "effective" specific heat C_v. However, we have found that the best numerical (theoretical) values of melting thresholds would result in slight discrepancy in fitting of the slope of shear wave arrival time versus incident peak laser intensity shown in Figure 3 for above-melting regime.

In order to verify the hypothesis for the effect of molten pool formation on the shear wave arrival delay we plot in Figure 3 measured shear wave arrival times versus incident laser peak intensities for all four metals along with two used models: (1) "FEM model" taking into account surface and volumetric sources in thermoelastic and melting regimes and (2) "Surrounding source model" describing melting regime based on simplistic right-triangle geometry due to only *ring surface sources* surrounding the molten pool. To better visualize the process of shear acoustic waves propagation, these two models are also schematically represented in Figures 4a and 4c for FEM model and in Figure 4b for "Surrounding source model".

TABLE I. Experimentally measured and theoretically predicted nanosecond laser pulse-induced melting thresholds for four refractory metals.

Metal	Experimental (I_{melt}^{exp}) (MW/cm^2)	Theoretical (I_{melt}^{G}) (MW/cm^2)	Theoretical ($I_{melt}^{t_{shear\ delay}}$) (MW/cm^2)	Poisson's ratio[34]
Nb	94	95	102	0.40
Mo	101	100	110	0.31
Ta	114	120	122	0.34
W	134	143	147	0.28

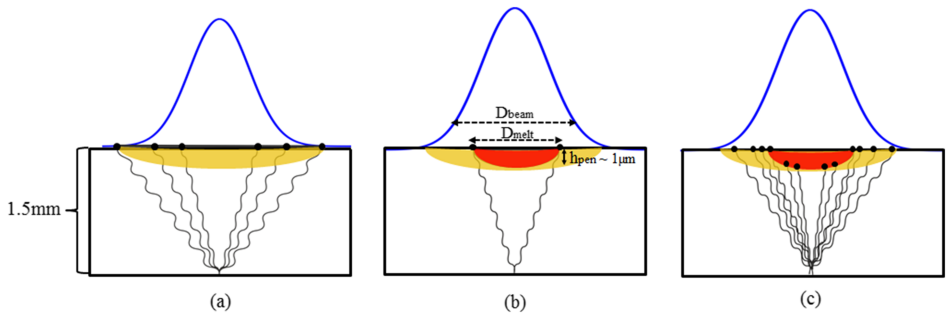

FIG. 4. A schematic (not scaled) diagram depicts shear waves generation and propagation to detection point from (a) all surface sources used in "FEM model" model describing thermoelastic regime, (b) only "ring" surface sources surrounding "red" molten pool used in "Surrounding source model" describing melting regime and (c) all surface and volumetric sources surrounding the molten pool in "FEM model" describing melting regime. The diameter of the laser beam D_{beam} ~ 900 μm resulting in maximum molten pool diameter D_{melt} ~ 600 μm is much larger than maximum molten pool depth Z_{melt} ~ 0.7 μm and maximum heat penetration depth h_{pen} ~ 1μm. Orange color relates to heat affected region.

It should be emphasized that calculated molten pool radii (maximum of 300 μm) are *much larger* than corresponding depths of heat penetration (~ 1 μm), which in turn are greater than corresponding depths of molten mass (~ fractions of μm). Additionally, the increase of the laser beam diameter in FE model leads to the increase of shear wave arrival delay. This explains that for laser peak intensities exceeding the melting threshold the shear waves are inhibited inside the molten pool and preferentially generated in the heat affected metal zone surrounding the molten mass which results in a delay of shear wave arrival time. They can also be generated inside the solid material just below the melting front, but shear waves arriving from the annular periphery are weighted more heavily, as depicted in the diagram of Fig. 4c. One should note that, because of symmetry, at the exact axis of the laser beam the shear wave with k vector normal to the surface cannot be excited.[35–37] Therefore, shear wave arriving at the opposite side of the plate is the sum of shear waves with different k-vectors emitted from the point sources near the axis of the beam.

To further analyze our measured results on laser pulse-induced phase transition we plot measured and theoretically calculated *relative* time delay of shear wave arrivals (along with listed handbook melting point temperatures) versus incident laser peak intensities in Figures 5 (a) and 5 (b), respectively. The shear wave transient time delay generally tends to get longer for less refractory metals than for higher refractory metals at the same peak intensity above melting thresholds of these metals. This trend is especially pronounced if we compare metals with highest melting point (W) and lowest melting point (Nb). Although the slopes for Ta and Mo were found to be alternating, but corresponding shear wave arrival times were observed to be longer than for W and shorter than for Nb.

V_{melt} (in μm/ns) in Fig. 5 (c) is calculated as a ratio of maximum molten pool radius R_{melt}^{max} in the radial plane of the sample to the time it takes to form this molten pool during laser pulse interaction with metals. R_{melt}^{max} is evaluated for different incident laser peak intensities $I_{peak}(T)$ by keeping track of isotherms corresponding to the melting temperatures, which in turn correspond to the fraction $a(T) = 1$ of molten mass in the solid-melt binary mixture.

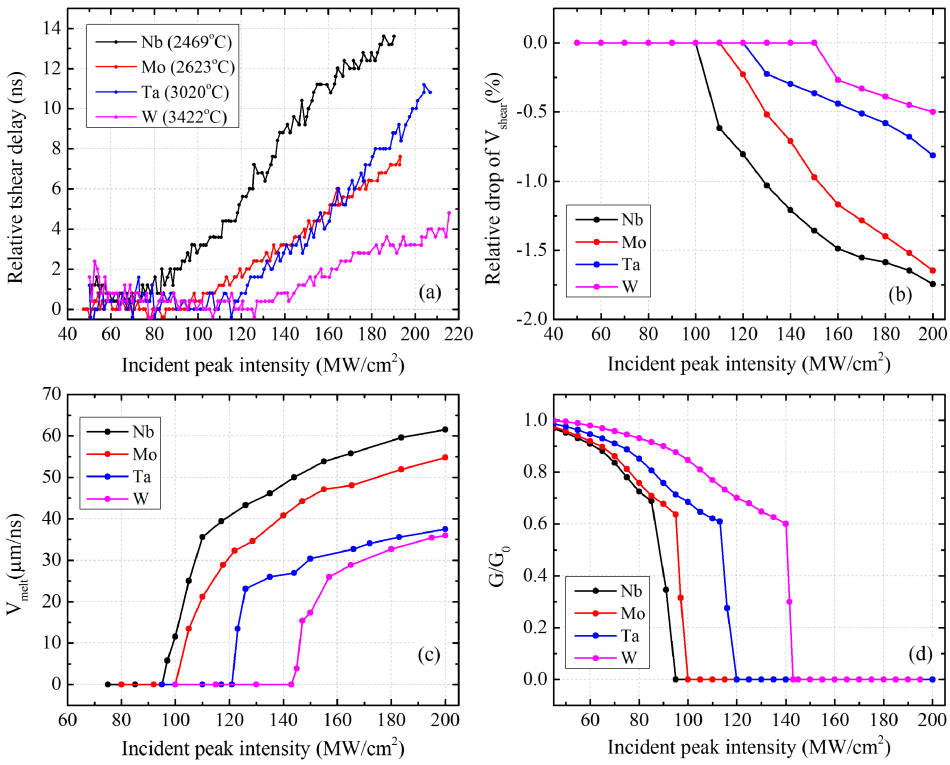

FIG. 5. Incident laser peak intensity-dependent (a) measured and (b) FEM calculated *relative* shear wave time delays as a function of incident peak intensity, (c) radial velocity of the melting front propagation and (d) shear modulus of the laser-irradiated metals for different refractory metals normalized to their shear modulus in thermoelastic regime.

The velocity of melting front propagation along radial direction (~ tens of μm/ns) is much greater than the sound velocity (~ few μm/ns). However, there is no contradiction with causality principle since melt front propagation in the radial plane of the sample surface is caused not by the heat conduction, but by its direct exposure to the laser heat flux. The melt front propagation velocity is like a phase velocity which can exceed the sound speed. This goes in line with a similar concept in optics where a phase velocity of light wave may exceed the speed of light.

In Figure 5 (d) we assume that the shear modulus of the laser-irradiated metals drops down to zero during the phase transition, as expected from molten solid losing its rigidity.[38] It is necessary to note that, unless this condition is satisfied, there is no agreement between our experiment and numerical model, which proves that onset of melting is accompanied by vanishing of shear modulus, i.e. loss of shear rigidity within molten pool, resulting in the delay of shear wave arrivals observed in our experiment. We have also found that temperature dependence of some thermophysical parameters such as (C_v, k, α) had little effect on the convergence of FEM results with those of experiment except density and first Lame coefficient which have to be changed.

In Table I for theoretically predicted melting thresholds we list corresponding threshold values predicted by relative shear wave delay time ($I_{melt}^{I_{shear\ delay}}$) and by the vanishing of shear modulus (I_{melt}^{G}) of within laser-irradiated metals. As it can be seen, there is a small difference between these two values. Shear modulus G drops to zero at the onset of melting at $T = T_m$+10 K in the center of the laser beam irradiated area leading to negligibly small molten pool. The pulse energy needed to form this molten mass, however, will be smaller than that which is necessary for the delay of the shear wave arrival time. To numerically resolve the time shift in the shear wave arrivals, it is necessary to generate estimated molten pool with the size of ~ 50 μm which is much larger than heat penetration depth. However, to get to this spatially extended molten mass it requires input of more pulse energy compared to that which is sufficient for vanishing of G. Therefore, $I_{melt}^{G} < I_{melt}^{I_{shear\ delay}}$.

I_{melt}^{G} was found to be closer to the experimental threshold value (I_{melt}^{exp}) since shear modulus represents more thermophysical nature of materials under dynamic high temperature transformation across laser affected region and through the laser-unaffected remaining solid mass of the plates. Further studies, such as *in-situ* thermal radiation spectral pyrometry and monitoring of surface acoustic waves within laser-heated metal regions, will be needed in order to have more comprehensive understanding of thermophysical nature of refractory solids under localized, rapid high temperature melting.

Comparing I_{inc}-dependent measured shear wave arrival times (Figure 5 (a)) with measured absolute shear amplitude displacements and shear/compressional amplitude ratios[39] displayed in Figure 6, we observe *featureless* shear amplitude behavior when $I_{inc} = I_{melt}$. However, in Figure 6 for bulk metals having lower melting points we clearly observe overall enhancement of the shearing

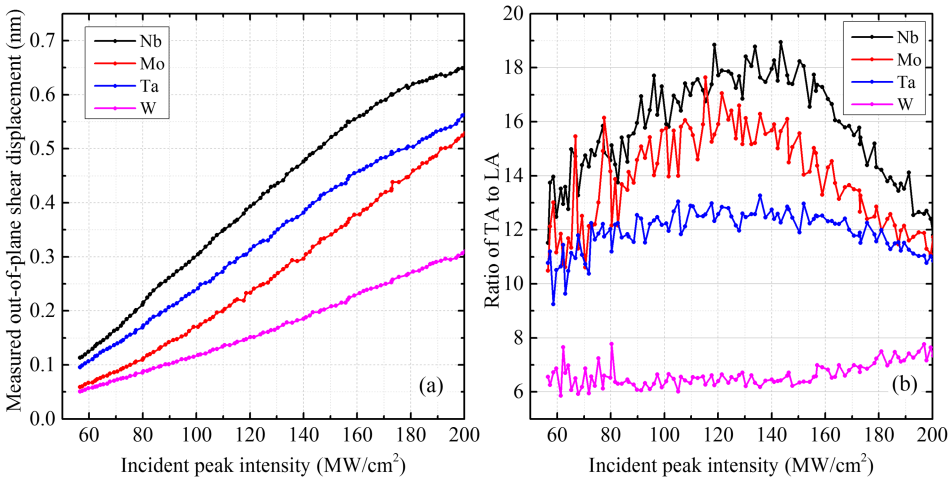

FIG. 6. (a) Measured out-of-plane shear wave displacement as a function of I_{inc} and (b) amplitude ratio of TA and LA steps as a function of I_{inc}.

amplitude behavior, attributed to the increase of Poisson's ratios,[5,34,39,40] the handbook values of which we also list in Table I.

V. CONCLUSION

Nanosecond laser peak intensity melting thresholds in Nb, Mo, Ta and W refractory metals have been determined experimentally by means of automated control of incident laser pulse energy and real-time detection of bulk ultrasonic waves using two-wave mixing photorefractive interferometry. Experimental results were found to be in good agreement with our FEM based on fully coupled elastodynamic and thermal conduction governing equations implementing "effective heat capacity" method, optimized spatial discretization and time-stepping, and also shear modulus vanishing in molten region. Observed trend in the increased melting thresholds for given refractory metals is in agreement with the increase of their corresponding melting point temperatures.

Systematic increase in the transit time delay of acoustic shear waves with the increase of nanosecond laser pulse energy was clearly observed for all studied refractory solids which is impossible to observe in static and quasi-statistic laser melting regimes often used to examine materials at high temperatures during "thermal arrest". This transit time delay was found to be due to surface and volumetric acoustic sources surrounding laser-induced molten pool, progressing in the radial direction on a much larger spatial scale than the spatial extent to which molten pool and heat penetrate inside the metals and also due to vanishing of the shear modulus within the molten pool resulting in the distribution of thermoelastic sources surrounding the molten mass.

For above-melting regime, measured transit time delay of shear waves was more pronounced in metals having lower melting points which were attributed to faster rate of molten mass formation in the plane of laser irradiated metal surfaces. This rate was an order of magnitude higher than effective shear wave velocity of studied metals. In these low-T_{melt} metals shearing behavior (due to increased Poisson's ratio) in their bulk becomes substantially enhanced not just in terms of risen delay of shear wave arrival times across metals bulk at the onset of laser-induced surface melting, but also in terms of enhanced shear ultrasonic energy deposited to the bulk metal during both laser-induced thermoelastic and above-melting regimes.

Developed "all-optical" technique can be employed for remote, non-contact ultrasonic control of laser processing of refractories, such as advanced examination of nuclear reactor fuels in the melting regime with high spatio-temporal resolution.

ACKNOWLEDGMENTS

This research was funded by Nazarbayev University SST0142015 grant and target program No 0115PK03029 "NU-Berkeley strategic initiative in critical state of matter, advanced materials and energy sources" from the Ministry of Education and Science of the Republic of Kazakhstan.

[1] L. R. F. Rose, The Journal of the Acoustical Society of America **75**(3), 723 (1984).
[2] P. A. Doyle, Journal of Physics D: Applied Physics **19**(9), 1613 (1986).
[3] K. L. Telschow and R. J. Conant, The Journal of the Acoustical Society of America **88**(3), 1494 (1990).
[4] D. A. Hutchins, "Ultrasonic generation by pulsed lasers," *Physical Acoustics* (Academic Press, Inc., San Diego, 1988), pp. 21–123.
[5] S. J. Davies, C. Edwards, G. S. Taylor, and S. B. Palmer, Journal of Physics D: Applied Physics **26**(3), 329 (1993).
[6] J. W. Wagner, J. B. Deaton, and J. B. Spicer, Applied Optics **27**(22), 4696 (1988).
[7] L. F. Bresse and D. A. Hutchins, Journal of Applied Physics **65**(4), 1441 (1989).
[8] C. B. Scruby, R. J. Dewhurst, D. A. Hutchins, and S. B. Palmer, "Laser generation of ultrasound in metals," *Research Techniques in Nondestructive Testing* (Academic Press, New York, 1982), pp. 281–327.
[9] L. Wu, J. C. Cheng, and S. Y. Zhang, Journal of Physics D: Applied Physics **28**(5), 957 (1995).
[10] T. W. Murray and J. W. Wagner, Journal of Applied Physics **85**(4), 2031 (1999).
[11] M. Dubois, F. Enguehard, L. Bertrand, M. Choquet, and J. P. Monchalin, Applied Physics Letters **64**(5), 554 (1994).
[12] H. Hebert, F. Vidal, F. Martin, J. C. Kieffer, A. Nadeau, T. W. Johnston, A. Blouin, A. Moreau, and J. P. Monchalin, Journal of Applied Physics **98**(3), 033104–1 (2005).
[13] M. Mesaros, O. E. Martínez, G. M. Bilmes, and J. O. Tocho, Journal of Applied Physics **81**(2), 1014 (1997).
[14] V. Gusev, A. A. Kolomenskii, and P. Hess, Applied Physics A **61**(3), 285 (1995).
[15] A. A. Ionin, S. I. Kudryashov, L. V. Seleznev, D. V. Sinitsyn, A. F. Bunkin, V. N. Lednev, and S. M. Pershin, Journal of Experimental and Theoretical Physics **116**(3), 347 (2013).

[16] S. J. Reese, Z. N. Utegulov, F. Farzbod, R. S. Schley, and D. H. Hurley, Ultrasonics **53**(3), 799 (2013).
[17] A. G. Every, Z. N. Utegulov, and I. A. Veres, Journal of Applied Physics **114**(20), 203508 (2013).
[18] A. G. Every, Z. N. Utegulov, and I. A. Veres in *AIP Conference Proceedings: Review of Progress in Quantitative Nondestructive Evaluation*, edited by D. E. Chimenti and L. J. Bond, (American Institute of Physics, Melville, New York, 2015), pp. 1350-1359.
[19] I. A. Veres, Z. N. Utegulov, and A. G. Every in *IEEE International Ultrasonics Symposium IUS-2014, Chicago, IL, USA, September 3 – 6 2014*, (IEEE Xplore), pp. 2474–2477.
[20] S. Rekhi, J. Tempere, and I. F. Silvera, Review of Scientific Instruments **74**(8), 3820 (2003).
[21] C. Ronchi and M. Sheindlin, International Journal of Thermophysics **23**(1), 293 (2002).
[22] D. Manara, R. Böhler, K. Boboridis, L. Capriotti, A. Quaini, L. Luzzi, F. De Bruycker, C. Guéneau, N. Dupin, and R. Konings, Procedia Chemistry **7**, 505 (2012).
[23] F. De Bruycker, K. Boboridis, R. J. M. Konings, M. Rini, R. Eloirdi, C. Guéneau, N. Dupin, and D. Manara, Journal of Nuclear Materials **419**(1), 186 (2011).
[24] A. Cezairliyan and F. Righini, Metrologia **33**, 299 (1996).
[25] H. Hu and S. A. Argyropoulos, Modelling and Simulation in Materials Science and Engineering **4**(4), 371 (1996).
[26] P. Zhang, C. F. Ying, and J. Shen, Ultrasonics **35**, 233 (1997).
[27] F. F. Schmidt and H. R. Ogden, "The engineering properties of tungsten and tungsten alloys," Rept. No. DMIC-191, Battelle Memorial Inst., (1963).
[28] E. P. Mikol, "The thermal conductivity of molybdenum over the temperature range 1000-2100°F," Rep. No. ORNL-1131, Oak Ridge National Laboratory, (1952).
[29] I. V. Savchenko and S. V. Stankus, Thermophysics and Aeromechanics **15**(4), 679 (2008).
[30] E. M. Savitskii and G. S. Burkhanov, *Physical Metallurgy of Refractory Metals and Alloys* (Consultants Bureau, New York, 1970).
[31] B. F. Pouet, R. K. Ing, S. Krishnaswamy, and D. Royer, Applied Physics Letters **69**(25), 3782 (1996).
[32] https://www.webelements.com/periodicity/melting_point/.
[33] J. Bovatsek, A. Tamhankar, R. Patel, N. M. Bulgakova, and J. Bonse, "Effects of pulse duration on the ns-laser pulse induced removal of thin film materials used in photovoltaics," Proc. SPIE 7201, Laser Applications in Microelectronic and Optoelectronic Manufacturing VII, 720116 (2009).
[34] https://www.webelements.com/periodicity/poissons_ratio.
[35] T. Pezeril, P. Ruello, S. Gougeon, N. Chigarev, D. Mounier, J.-M. Breteau, P. Picart, and V. Gusev, Physical Review B **75**(17), 174307 (2007).
[36] T. Pezeril, C. Klieber, S. Andrieu, and K. A. Nelson, Physical Review Letters **102**(10), 107402 (2009).
[37] T. Pezeril, [INVITED] Optics & Laser Technology **83**, 177–188 (2016).
[38] M. H. Nadal, C. Hubert, and R. Oltra, Journal of Applied Physics **106**, 024906 (2009).
[39] C. B. Scruby, R. J. Dewhurst, D. A. Hutchins, and S. B. Palmer, Journal of Applied Physics **51**(12), 6210–6216 (1980).
[40] R. J. Dewhurst, D. A. Hutchins, S. B. Palmer, and C. B. Scruby, Journal of Applied Physics **53**(6), 4064–4071 (1982).